journal of the mechanical behavior of biomedical materials 152 (2024) 106467

Contents lists available at ScienceDirect

Journal of the Mechanical Behavior of Biomedical Materials

journal homepage: www.elsevier.com/locate/jmbbm

An interferometric-based tensile tester to resolve damage events within reconstituted multi-filaments collagen bundles

Hessameddin Yaghoobi [a], Chloe Tremblais [a], Alex Gareau [a], Matthieu Cointe [a], Alexey B. Tikhomirov [a], Laurent Kreplak [a,b], Daniel Labrie [a,*]

[a] Department of Physics & Atmospheric Science, Dalhousie University, Halifax, Nova Scotia, B3H 4R2, Canada
[b] School of Biomedical Engineering, Dalhousie University, Halifax, Nova Scotia, B3H 4R2, Canada

ARTICLE INFO

Keywords:
Tensile testing
Plastic damage
Force microscopy
Michelson interferometry

ABSTRACT

Understanding how mechanical damage propagates in load-bearing tissues such as skin, tendons and ligaments, is key to developing regenerative medicine solutions for when these tissues fail. For collagenous tissues in particular, damage is typically assessed after mechanical testing using a broad range of microscopy techniques because standard tensile testing systems do not have the time and force sensitivity to resolve mechanical damage events. Here we introduce an interferometric detection scheme to measure the displacement of a cantilever with a resolution of 0.03% of full scale at a sampling rate of 5000 samples/s. The system is validated using collagen fibers engineered to mimic mammalian tendons. The system can detect sudden decrease in force due to slippage between collagen filaments, one to five microns in diameter, within a fiber in air. It can also detect yield events associated with local collagen unfolding or sliding within collagen fibrils within a fiber in liquid. This is opening the road to the sub-failure study of damage propagation within a broad range of hierarchical biomaterials.

1. Introduction

Collagen is one of the main constituent of mammalian connective tissues such as skin, tendon, and bone. In mice, Collagen represents 20–50 % of the total protein content of these three tissues (Tarnutzer et al., 2023) and is responsible for their outstanding mechanical properties. To achieve their load-bearing function, collagen triple helices are assembled into fibrils with diameters between 50 and 500 nm, and a length that can easily reach more than hundred micrometers in tendons (Revell et al., 2021). Measuring the tensile properties of single collagen fibrils is both key to understand their biological function and experimentally challenging (Andriotis et al., 2023). Qualitatively, the stress-strain curve of a single collagen fibril is composed of three phases, an "elastic" phase followed by a yield phase and a strain-hardening phase (Svensson et al., 2013). However there is no consensus on the value of mechanical parameters for each phase. This is due in part to variations in collagen sources and age of animals used (Andriotis et al., 2023). It is also due to the difficulty in assessing fibrils dimension before testing and the difficulty in measuring forces up to a few microNewtons with enough accuracy using either atomic force microscope cantilevers or microelectromechanical sensors (Andriotis et al., 2023). Yet, there is some agreement regarding deformation mechanisms within fibrils and the fact that unfolding of collagen triple helices occurs during the yield phase (Andriotis et al., 2023). Unfolding can be detected after tensile testing at the single fibril- or tendon-levels using fluorescent peptides that bind to unfolded regions of a single collagen alpha-chain but not to intact triple helices (Iqbal et al., 2019; Li et al., 2023; Lin et al., 2020; Quigley et al., 2018; Zitnay et al., 2017). The capacity of collagen fibrils to absorb mechanical energy by triple helices unfolding is one of the mechanisms responsible for the toughness of both skin (Yang, 2015) and tendon (Veres and Lee, 2012).

For tendons, the development of tendinopathies is generally associated with mechanically-induced damage at some level of the tissue hierarchy from fascicles (⌀ >100 μm) to collagen fibers (⌀ >10 μm) to fibrils (⌀ > 0.5 μm) (Snedeker and Foolen, 2017). Currently, there is no consensus regarding the mechanism for the accumulation or nature of damage (Snedeker and Foolen, 2017). There is mounting evidence that tendons that are loaded to failure (Veres and Lee, 2012), loaded past the yield point (Lin et al., 2020; Zitnay et al., 2017), loaded cyclically past the yield point (Veres et al., 2013) or loaded cyclically below the yield point (Herod et al., 2016) show accumulation of collagen fibril-level damage in the form of kinks and/or regions where triple helices

* Corresponding author.
E-mail address: Daniel.Labrie@dal.ca (D. Labrie).

https://doi.org/10.1016/j.jmbbm.2024.106467
Received 13 December 2023; Received in revised form 9 February 2024; Accepted 15 February 2024
Available online 16 February 2024

unfolding occurred (Baldwin et al., 2019; Veres and Lee, 2012; Zitnay et al., 2017). However it is unclear whether the damage is due to shear stresses between short collagen fibrils (Szczesny and Elliott, 2014; Zitnay et al., 2017) or due to direct loading of continuous collagen fibrils in tension (Hijazi et al., 2019; Svensson et al., 2017) or compression (Chambers et al., 2018; Peacock et al., 2020). Being able to pinpoint the moment when damage occurs within a tendon during a loading/unloading cycle would significantly improve our understanding of the onset of tendinopathies. So far all damage assessments are carried out after the fact using a wide range of microscopy techniques and point towards localized damage sites along the tendon length and across its section (Szczesny et al., 2018). In addition, standard tensile testers do not have the sensitivity, dynamic range or acquisition rate required to unambiguously observe the mechanical signature of localized damage events in tendons even so published data point to their potential existence (see Fig. S3 in (Herod et al., 2016)).

In this work, we build and validate a microtensile tester suitable for collagen fibers which uses a Michelson interferometer and a HeNe laser to measure the deflection of a quartz cantilever with an acquisition rate of 5000 samples/s and a force resolution better than 0.03% of full scale. To test our instrument, we use a recently developed contact drawing technique (Verma et al., 2022; Yaghoobi et al., 2023) to fabricate tendon-like collagen bundles designed specifically to maximize the chance of observing damage events induced by either shearing or stretching of collagen molecules. Overall the system is able to accurately detect force discontinuities indicative of local rupture or yield event for collagen bundles tested in air and in liquid. This is opening the road for the direct measurement of damage events in collagen fibres and other protein-based materials.

2. Material and methods

2.1. Fabrication of engineered collagen fibers

The preparation of the PEO-collagen solution and the production of collagen fiber bundles was adapted from a previous study (Yaghoobi et al., 2023). Briefly, PEO powder (8 MDa; Sigma Aldrich) was dissolved with pepsin solubilized collagen type I (~6 mg/mL in 0.01 M HCl; Collagen Solutions) to achieve a solution with a 1:1 PEO-collagen weight ratio in 20 mM acetic acid, with a final weight concentration of 6.75%.

To prepare fibers, the PEO-collagen solution was spread on a flat rectangular substrate. An array of cylindrical pins was then used to produce PEO-collagen filaments by contacting the pin array with the viscous solution and then pulling the pin array away from the rectangular plate (Yaghoobi et al., 2023). The pulling speed must be above a critical value that depends on the length of the pull and the viscoelastic properties of the solution (Chowdhry et al., 2021; Palit et al., 2022). In this case, each filament was around 10 cm long, with a diameter between 1 and 5 μm and the pulling speed was around 0.3–1 m/s. The filaments were gathered by their ends, twisted 4–5 times, and rolled into a tighly consolidated bundle containing around 50–100 filaments. Note that this fabrication process is different from the one used by Yaghoobi et al., which had a UVC treatment step after the removal of PEO, to create crosslinks within and between filaments (Yaghoobi et al., 2023). Here, the PEO was not removed so crosslinks were only created within each filament, producing a fiber that mimics mammalian tendon hierarchical structure.

2.2. Characterization of engineered collagen fibers

The collagen filaments and bundles were imaged using a Nikon Eclipse Ti optical microscope (Nikon Instruments). All images were analyzed using ImageJ (www.imagej.net). In addition, a few bundles were rinsed for 30 min in Phosphate Buffered Saline (PBS) aqueous solution, rinsed with water, dried in a nitrogen stream and double-taped on a glass-slide for imaging by atomic force microscopy (AFM). We used a Bioscope Catalyst AFM (Bruker) mounted on an IX-71 inverted microscope (Olympus) to image the surface of dry bundles after PEO removal. The AFM was operated in ScanAsyst mode using ScanAsyst fluid + cantilevers (nominal spring constant 0.7 N/m, Bruker). The cantilevers were oscillating off-resonance at a frequency of 1 kHz and an amplitude of 150 nm. The applied force was fixed between 5 and 20 nN and the scan rate was 0.5 Hz. All images were post-processed using Gwyddion (www.gwyddion.net).

2.3. Interferometric tensile testing

The general approach used to measure the stress – strain relationship of filaments and bundles consists of attaching a filament (bundle) between a cantilever and a translation stage. The force acting on the filament (bundle) is given by the product of the cantilever deflection and its spring constant while the filament's elongation is given by the difference in displacement between the translation stage and cantilever. The stress is calculated using the cantilever force divided by the fiber (bundle) cross sectional area using its diameter measured in air. The strain is calculated using the ratio of the fiber elongation divided by its original unstretched length. A schematic diagram of the experimental apparatus is depicted in Fig. 1. A 22.5 mW HeNe laser (JDS Uniphase) is shone through a 25 mm focal length achromatic doublet lens (Edmund Optics) and reflected by two plane mirrors (Edmund optics) onto a 450 mm focal length achromatic doublet lens to collimate the beam to a diameter of 2 cm. The laser beam is incident on a Michelson interferometer consisting of a non-polarizing cube beam splitter (Edmund optics) where part of the beam is reflected onto a fixed (reference) mirror (Edmund optics) while the remaining part of the beam is transmitted through the beam splitter to a moving mirror (Edmund optics) mounted on a translation stage and to a cantilever. The linear translation stage Model M-462-X-M (Newport) has 25 mm travel distance. The custom made cantilever consists of either a 0.52 mm (or 0.95 mm) thick by 4.95 mm (or 4.96 mm) wide by 75 mm long quartz strip (Technical Glass Products) mounted rigidly at one end onto a 25 mm diameter stainless steel rod (shown in Fig. 2b). The other end is attached onto an Aluminium support referred below as the cantilever foot and is free to move. The lower part of the cantilever has Aluminium evaporated on it to act as a mirror. The laser beam is reflected by the moving mirror and cantilever mirror back to the beam splitter where the beam is recombined with the reference beam from the fixed mirror. The recombined laser beam interferes at the detector plane consisting of three 0.5 mm diameter Silicon photodiodes (Edmund optics). The laser beam reflected by the moving mirror is monitored by one Silicon photodiode while the beam reflected at the bottom and top of the cantilever is detected by the bottom and top photodiode, respectively. Note that this beam goes through a – 50 mm plano-concave cylinder lens for increased 2X fringe magnification before reaching the photodetectors. In addition, the quartz cantilever is of sufficient flatness (within 4.4 λ per 25.4 mm) capable of producing a single interference fringe at the output of the interferometer. The photodiode current outputs are amplified using custom transimpedance low frequency pass amplifiers with a 3 dB frequency of 800 Hz and digitized using a data acquisition system USB – 6281 (National Instruments). The position of the linear translation stage is set using a SM – 25 μm head (Newport) coupled to a 5 – phase stepping motor model PKE544AC (Oriental Motor) controlled using a new pentagon microstep driver model RKSD503 – A (Oriental Motor) and universal controller model SCX11 (Oriental Motor). The stepping motor system was set to 125,000 steps per revolution mitigating vibrations related to stepping. The programmed translation stage speed used in this work was 10 μm/s to further minimize any motor induced vibrations. Custom programs designed in LabVIEW version 2019 (National Instruments) were developed to control the stepping motor and to perform data collection and analysis. Oversampling of the amplifier outputs was carried out at 5000 samples per second to perform post signal averaging. The AC signal measured at the three amplifier outputs were converted into a

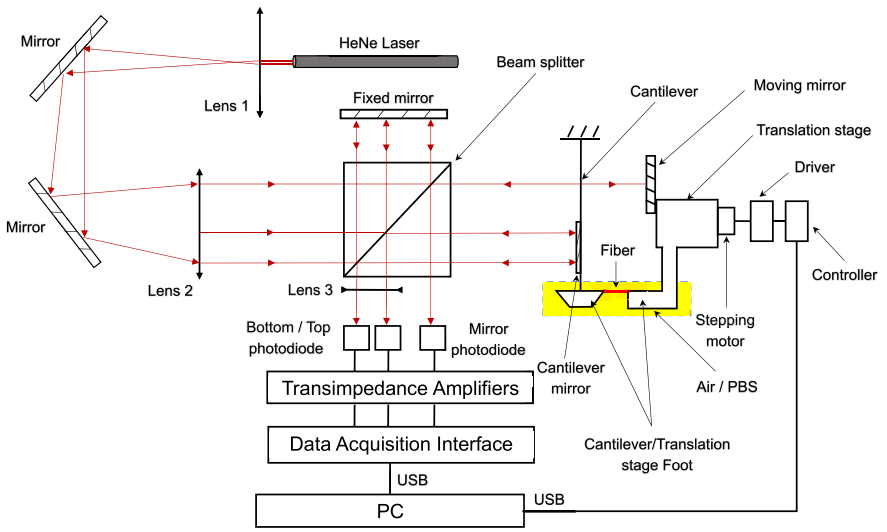

Fig. 1. Schematic of the interferometric tensile tester. The filament (bundle) is glued on the cantilever and translation stage foot. The feet displacements are measured using the cantilever and moving mirrors.

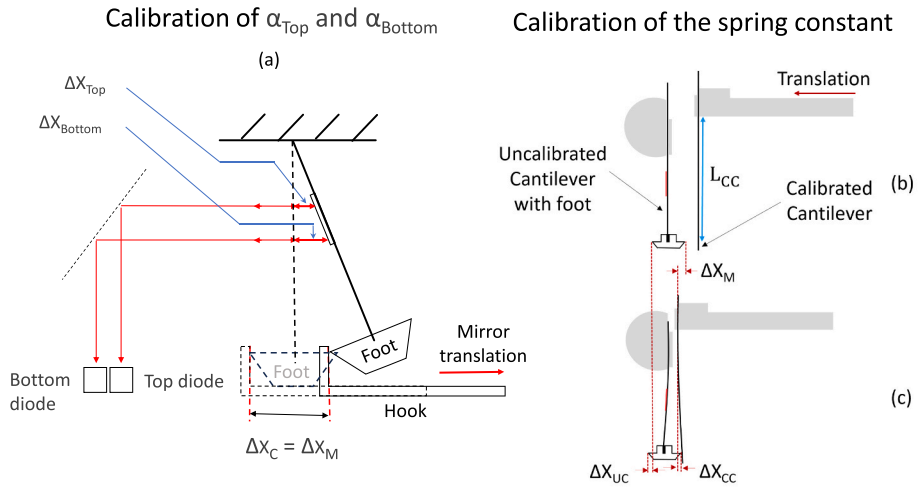

Fig. 2. Experimental geometries used to measure α_{Top} and α_{Bottom} (a), and the cantilever spring constant with the foot (b) and (c) using measurements of the mirror and cantilever foot displacements, and the spring constant of a uniform cantilever without a foot.

displacement of the cantilever and translation stage foot using signal processing. Further details are given in the supplementary materials.

The separation between the cantilever and translation stage feet ends was set at 5.0 mm. The ends of tested filament and bundle were attached to the end of the cantilever foot and translation stage foot using cyanoacrylate glue. The glue was allowed to cure for 3 h before testing. Consequently, the initial unstretched length of the filaments and bundles was 5.0 mm. If required, a 10 cm diameter plastic dish was placed underneath the two feet to submerge the bundle in PBS aqueous solution for 30 min before testing.

2.4. Calibration of the cantilever

Fig. 2 (a) depicts the geometry used to determine the cantilever foot displacement, ΔX_C, in terms of the cantilever displacement measured by the bottom, ΔX_{Bottom}, and top, ΔX_{Top}, photodiode, respectively. A hook was attached to the translation stage foot so that the mirror displacement, ΔX_M, was set equal to ΔX_C. A linear relationship was found between ΔX_C and ΔX_{Bottom} and, ΔX_C and ΔX_{Top}, where the proportionality constants, α_{Bottom} and α_{Top}, were determined for each cantilever used in this work. For the 0.95 mm (0.52 mm) thick cantilever α_{Bottom} and α_{Top} were 4.236 (3.607) and 5.276 (4.490), respectively. Fig. 2 (b) displays the geometry used to measure the cantilever spring constant with its foot. A second cantilever was mounted on the translation stage with dimensions similar to those of the uncalibrated cantilever. As shown in Fig. 2 (c), the second cantilever was brought into contact with the first one (Jericho and Jericho, 2002). From the measurement of ΔX_M and the displacement of the uncalibrated cantilever, ΔX_{UC}, the displacement of the calibrated cantilever, ΔX_{CC}, can be calculated. Using simple beam bending mechanics (Lifshitz et al., 1986), the spring constant of the calibrated cantilever is given by $k_{CC} = ¼\ Ew(t/L_{CC})^3$ where E, w, t, and L_{CC} are the Young's modulus of quartz with a value of 72 GPa, width, thickness, and length of the quartz cantilever in contact with the foot, respectively. Using static equilibrium, the values of the spring constant for the 0.52 mm and 0.95 mm thick cantilever were 72 ± 3 N/m and 485 ± 8 N/m, respectively. The values are to within 5 % in agreement with the calculation of the spring constants of the cantilevers with foot using finite element analysis.

2.5. Statistical analysis

One factor ANOVA, followed by Tukey tests, were used to determine

if there were statistical differences in the mechanical properties (elastic modulus and maximum strain) of filaments and bundles in air and, bundles in air and in PBS aqueous solution ($p = 0.05$).

3. Results

For this study we measured the stress-strain curve of five UVC crosslinked PEO-collagen filaments in air with diameters between 1.2 and 4.4 μm, and of seven PEO-collagen bundles (three bundles in air and four bundles in PBS solution) with diameters between 12 and 27 μm. The estimated elastic modulus and strain at rupture for the Filaments and Bundles in air and PBS aqueous solution are shown in Table 1. Note that it was not possible to measure the stress-strain curve of single filaments in PBS solution. The filaments broke as they were immersed in PBS solution because of the exceedingly large force acting on the filaments generated between the solution surface tension and the micron-sized filaments. Representative optical images of a filament and bundles are presented in Fig. 3 (panels a–c). Not all bundles were well consolidated in air with loose filaments looping out of the bundles surface (for example, compare Fig. 3b and c), yet after washing all bundles appeared to consolidate (similar to Fig. 3c, but not shown). However AFM imaging revealed that after washing contacts between filaments is uneven with the presence of large gaps (Fig. 3d). AFM imaging also confirms that each filament is composed of a parallel array of thin collagen fibrils (Fig. 3e) as previously shown by Yaghoobi et al. (2023).

3.1. Tensile tester validation

To validate our interferometric tensile tester, we compared stress – strain curves acquired with our set-up with curves acquired on a home-built microtensile tester using a balance (Fig. 4) (Verma et al., 2022). In both cases, the stress strain curves have identical shape but vary in magnitude due to the inherent difficulty of accurately measuring filament diameters. Note that we display raw data showcasing the difference in the force resolution between the two systems. For the balance-based tester, the steps in stress are due to the instrument integration time which is in the 1 s range. In contrast the interferometric tester has transimpedance amplifiers with 3 dB frequency points of 800 Hz and an acquisition rate of 5000 samples/s and continuously monitors changes in position of the cantilever and the end of the specimen attached to the translation stage, at that frequency, as the specimen is being extended. This is best illustrated by looking at the raw signal

Table 1
Diameter, immersion medium, elastic modulus, and strain at rupture of filaments and bundles.

Fiber label	Diameter (μm)	Immersion medium	Elastic modulus (GPa)	Strain at breakage (%)
Filament 1	1.21	Air	8.2 ± 0.6^{a}	22.5 ± 0.1^{a}
Filament 2	1.48	Air	7.2 ± 0.6^{a}	23.2 ± 0.1^{a}
Filament 3	3.6	Air	9.3 ± 0.1^{a}	17.4 ± 0.1^{a}
Filament 4	1.4	Air	13 ± 1^{a}	20.3 ± 0.1^{a}
Filament 5	4.4	Air	4.5 ± 0.1^{a}	23.8 ± 0.1^{a}
Bundle 1	21.3	Air	3.0 ± 0.1^{b}	11.4 ± 0.1^{a}
Bundle 2	12.7	Air	2.2 ± 0.1^{b}	26.7 ± 0.1^{a}
Bundle 3	13.9	Air	1.9 ± 0.1^{b}	26.5 ± 0.1^{a}
Bundle 4	20.1	PBS	0.15 ± 0.01^{c}	21.7 ± 0.1^{a}
Bundle 5	21	PBS	0.19 ± 0.02^{c}	8.6 ± 0.1^{a}
Bundle 6	20	PBS	0.17 ± 0.01^{c}	13.9 ± 0.1^{a}
Bundle 7	27.3	PBS	0.09 ± 0.01^{c}	23.4 ± 0.1^{a}

Within each column different superscript letter indicates significant differences between fiber ($p < 0.05$).

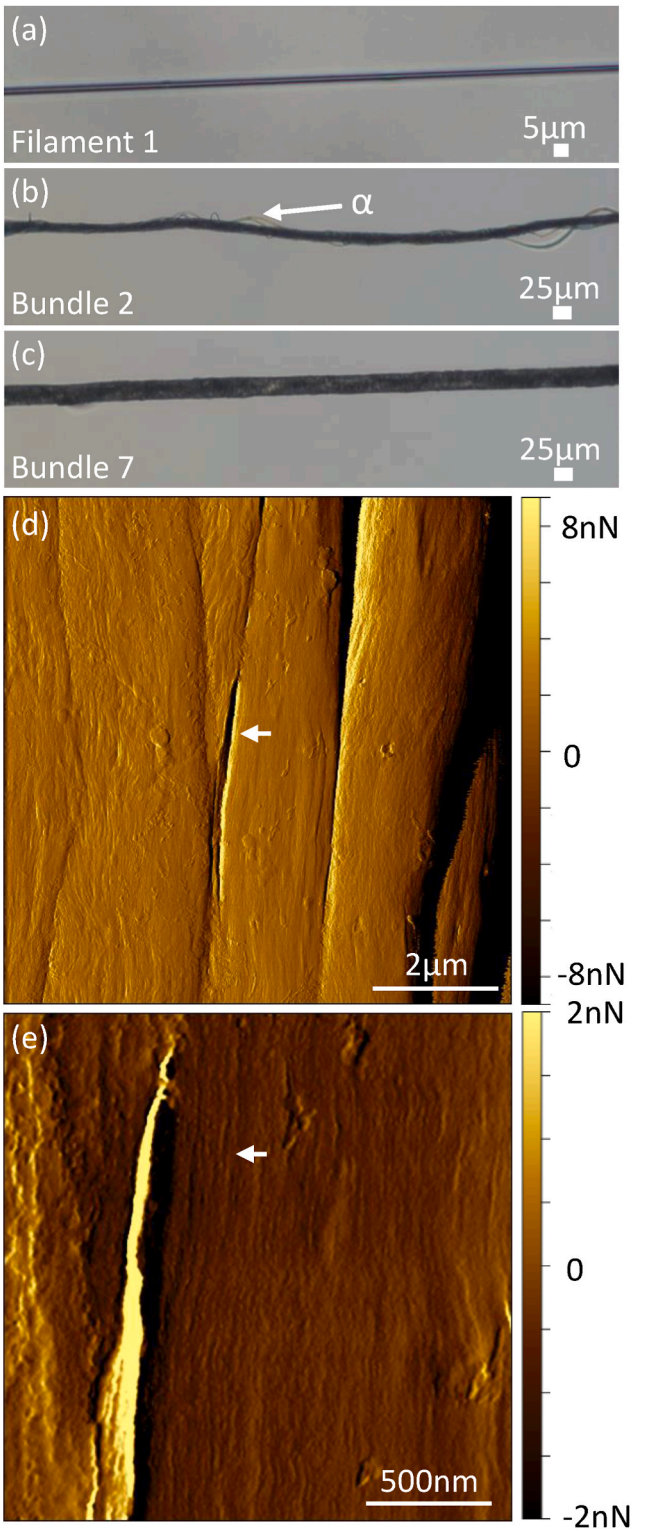

Fig. 3. Optical microscopy images of (a) Filament 1, (b) bundle 2 and (c) bundle 7. Filament 1 is of uniform diameter while bundle 2 is made with several filaments as shown by marker α. Bundle 7 has a non uniform diameter along its length. Atomic force microscopy images (error channel) of a bundle surface after immersion in PBS solution for 30 min revealing multiple filaments (d). The bundle axis is vertical on the images. Note the presence of gaps between filaments as exemplified by the arrow (d). The fibrils within each filament are also visible (arrows in (e)) as indicated by the vertical line structure within a single filament (Yaghoobi et al., 2023).

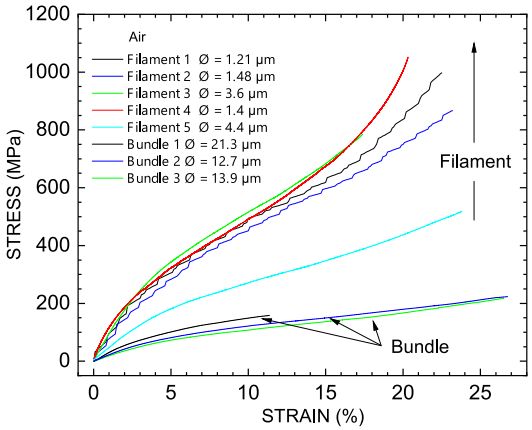

Fig. 4. Stress as a function of strain for Filament 1–5 and bundle 1–3 in air. Note that the maximum stress varies between 500 and 1100 MPa for the Filaments while it is between 160 and 220 MPa for the bundles. Filaments 1 and 2 were measured using a balance-based tensile tester.

acquired by all three diodes of the tester (Fig. 5). Even so our tester uses a stepper motor with no optical encoding, the position of the mirror mounted on the translation stage is measured in real-time allowing us to correct for non-uniformity in translation such as a very small, 0.22 μm, backlash of the translation stage occurring over the first 0.15 s of motion (Fig. 5a). The angular acceleration of the stepper motor over the first 0.5 s of motion until the motor reached its steady state angular velocity is also easily noticeable as a steady decrease of the period of oscillation of the light intensity up to 0.5 s after the start of data collection and thereafter the period is constant (Fig. 5a). Note that the separation between two successive extrema corresponds to a mirror displacement or equivalently to a translation stage foot displacement of $\lambda/2$ where $\lambda = 632.8$ nm is the emission wavelength of the HeNe laser. An example of the light intensities measured at the top and bottom diode (Fig. 1) during the extension of Bundle 2 (Fig. 4) is presented in Fig. 5 (b). Both oscillatory signals decrease in frequency over time as expected for a material that is softening under strain as seen in Fig. 4. The moment the bundle breaks, the two signals rapidly oscillate indicating that the cantilever is no longer attached to the bundle and oscillates freely at its natural frequency of about 96 Hz (Fig. 5b). Fig. 5 (c) is an expanded view of the two signals just before the bundle breaks. There are two visible rapid events marked α and β that can be attributed to a sudden disturbance of the bundle while events marked γ and δ indicate the beginning and complete rupture of the bundle, respectively (Fig. 5c). This example highlights the very high time resolution of the interferometric tester to sudden changes in force that are not easily displayed on the stress strain curve, yet clearly identifiable in the raw data.

3.2. Bundle testing in air and in PBS aqueous solution

Bundles measured in air have tensile properties significantly lower than the ones measured for single filaments (Table 1). This is likely due to the fact that the glue used to fix the end of the bundles did not penetrate fully into the material leading to most of the load being carried by filaments at the surface of the bundles. This effect is further enhanced by our bundle design where there is no covalent bonds between filaments allowing slippage to occur within the bundles or a subset of filaments to break as potentially shown by the rapid events marked α and β in Fig. 5 (c). A simple geometrical model of 50 or 100 filaments with the same uniform diameter along their length and where they are close packed predicts that if all the filaments are equally involved in the tensile measurement then the elastic modulus of the bundle is about 15 % or 18 % below that of a single filament. This is due to the estimation of the bundle diameter and where there is void between the filaments in the bundle. However, if only the outer filaments of the bundle participate in the tensile measurement because they are the only one glued together then the corresponding elastic modulus of the bundle is about one half or one third of that of a single filament. This estimate is in general agreement with the results shown in Table 1 for the elastic modulus of single filament and bundle in air. When immersed in PBS solution, the bundles release PEO into the buffer, leaving behind a collagen fibre with tensile properties which decrease sharply when hydrated as observed in collagen fibrils for example (Andriotis et al., 2018). They also tend to swell albeit inconsistanly. Note that the stress strain curves presented in Fig. 6 (a) use the cross-sectional area of the bundle before immersion to calculate the stress which likely results in an overestimate. Nonetheless, bundles in PBS solution are significantly much weaker than bundles measured in air and each stress strain curve shows small irregularities in the yield region, the most striking are highlighted for bundle 4 (Fig. 6a, markers α and β). These irregularities can be understood by looking at the averaged oscillatory signal associated with the top photodiode for bundle 4 (Fig. 6b). Both irregularities represent small yield events or kinks in the curve. The first event (Fig. 6, marker α) is the clearest of the two showing a sudden increase in the oscillation period followed after four periods by another sudden decrease in the oscillation period. The entire event occurs over only 2 % strain and would be undetectable with the balance based tester mentioned above. This type of event is not observed for bundle 2 in air (see Supplemental Fig. 3) where the period associated with the oscillatory signal varied monotonically with strain and no sudden change in period is observed.

4. Discussion

4.1. Interferometric tensile tester sensitivity

The main features of the interferometric tensile tester presented in this work are its force resolution and the fact that the raw signal measured is oscillatory in nature (Fig. 5). Michelson interferometry relies on measuring a sinusoidal signal produced by dark and bright fringes moving past a photodetector as the aluminized surface of the cantilever is deflected. As long as there is enough contrast between these fringes, the system can accurately detect a displacement of the order of a fraction of one laser wavelength for any amount of the cantilever's total deflection. We estimate that the minimum displacement we can robustly measure is $\lambda/8$ or 79 nm, this is based on the quality of the fringes in PBS solution (Fig. 6b). The total cantilever deflection is limited by the fringe visibility between dark and bright fringes measured by the active area of the Si photodiode. As the cantilever deflects, a larger number of fringes is incident on the photodiode active area. The photodetector measures the average intensity of all the fringes incident over its active area. As a result, the fringe visibility decreases with an increasing number of fringes on the photodetector and hence with increasing cantilever deflection. The plano-concave cylinder lens partially mitigate this effect by magnifying by $\times 2$ the fringe pattern on the detector plane. In our case for both cantilevers used in this study the maximum deflection that can be measured is 270 μm giving the tester a force resolution of 0.03% of full-scale. Note that the lowest measurable displacement, $\lambda/8$, is independent of the absolute cantilever deflection. This is a unique feature of Michelson interferometry compared to other sensing schemes such as Fabry-Perot based interferometric sensors (Zhu et al., 2023) or Fibre Bragg grating sensors (Sahota et al., 2020), that continuously monitor the physical quantity of interest, the intensity of the laser in the Fabry-Perot cavity or the wavelength of the light reflected by a grating, respectively. More generally, monitoring a slowly varying DC signal (DC versus AC in our case) makes other force sensing approaches less sensitive to small changes in force due to the time averaging required to achieve a sufficiently high signal to noise ratio (Svensson et al., 2018) to

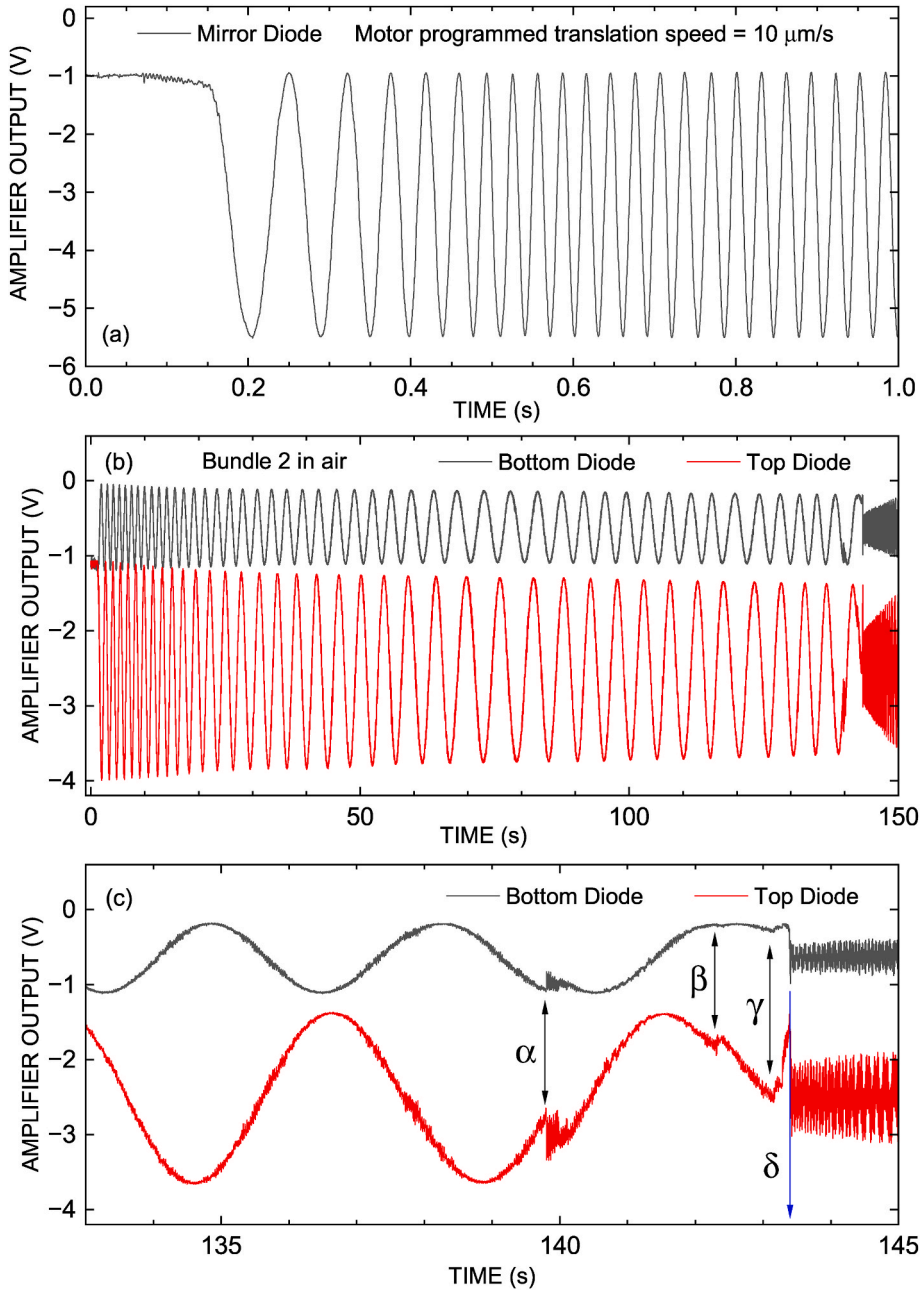

Fig. 5. Raw amplifier output signals from the mirror (a), Bottom and Top photodiode (b) and (c) collected using bundle 2 in air. The programmed translation stage speed was 10 μm/s. For clarity, the top photodiode data was shifted down by −1 V. In Figure (b) and (c) at t = 143.3 s, rapid cantilever oscillations are detected and are associated with the rupture of the bundle. In Figure (c), event α and β are associated with a sudden material disturbance within the bundle while event γ and δ are attributed to a gradual and then total rupture of the bundle.

detect a very small variation in signal superimposed onto a large background.

4.2. Interpreting collagen fiber damage events

The collagen fibers prepared for this study were specially designed to enable the observation of damage events. For single filaments tested in air (Figs. 3a and 4), there was no evidence of sudden damage events in the raw data as expected from the fact that PEO-collagen filaments are extremely uniform along their length as previously reported (Verma et al., 2022; Yaghoobi et al., 2023). Damage events were only observed at the bundle level both in air and in PBS solution (Figs. 5c and 6b).

In air, damage events were of two kinds, short instances were the force applied on the cantilever suddenly decreases allowing the cantilever to start oscillating close to its free frequency (Fig. 5c, markers α and β) and events where the effective stiffness of the bundle (the slope of the stress strain curve) decreases (Fig. 5c, marker γ). In filament bundles, the mechanical signature of a slippage event between filaments is an abrupt decrease in force (see (Ryu et al., 2015) for an example in carbon nanotube bundles), this is likely the explanation for the event α and β in Fig. 5 (c). The other event in Fig. 5 (c) occurs just before failure and is likely indicative of necking.

In PBS solution, the polymer quickly diffuses out of the bundles leaving behind a collagen fiber (Fig. 3d) composed of filaments that are held together by non-covalent interactions (Yaghoobi et al., 2023). At least at the surface filament-filament contacts are not continuous with the presence of gaps (Fig. 3e). However, considering that each filament spans the length of the bundle, the probability of slippage between

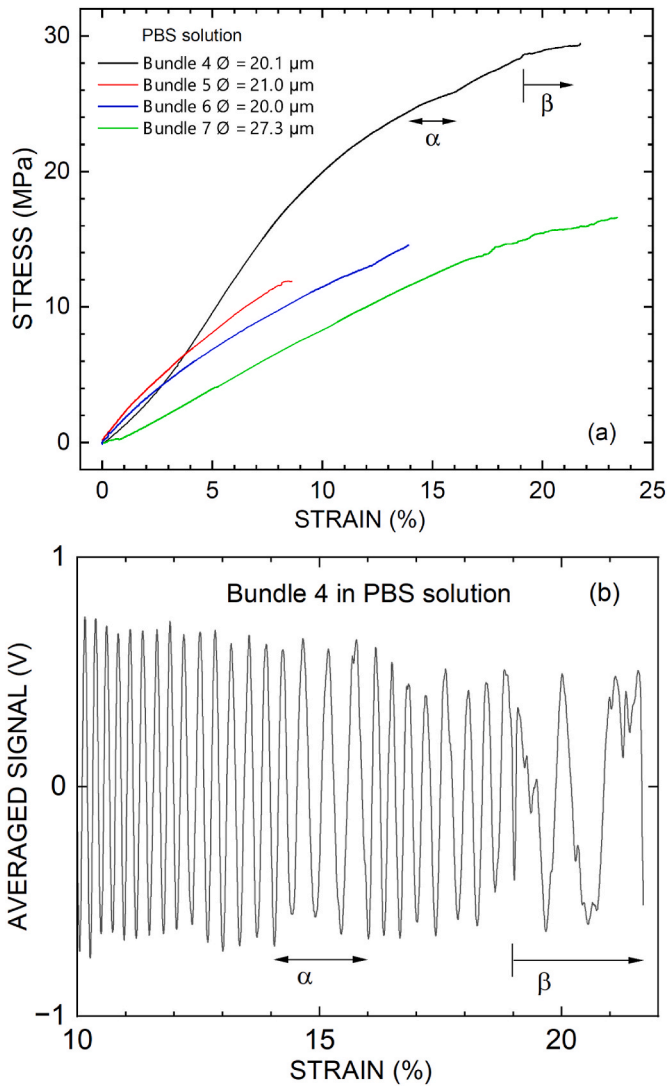

Fig. 6. Stress as a function of strain for bundle 4–7 in aqueous PBS solution (a) and averaged signal associated with the top photodiode as a function of strain for bundle 4 in solution. The maximum stress that a bundle can withstand is between 12 and 29 MPa. Note event α and β depicted in (a) are clearly displayed in the oscillatory photodiode output in (b).

filaments is likely very low and we did not observe sudden events like the one presented in Fig. 5 (c) markers α and β. Instead, we observed a clear yield event (Fig. 6b, marker α) where the effective stiffness of the bundle where $E_{eff} = dS/d\varepsilon$ suddenly dropped by half before returning to its pre-yield level. This can be assessed by counting the number of fringes over two percent strain, four fringes in this case, before and after the event which has the same number of fringes over 2 % strain (Fig. 6b, marker α). This kind of softening-stiffening transition is actually a characteristic of the stress strain curve of single collagen fibrils extracted from human, rat and bovine tendons (see ((Andriotis et al., 2023) for review). Typically the pre-yield and post-yield stiffness of single fibrils is very similar (Andriotis et al., 2023) consistent with the yield event we observed. Based on the geometry of our bundles and the fact that each filament is an array of UV crosslinked fibrils (Yaghoobi et al., 2023) then the yield event (Fig. 6b, marker α) is likely due to localization of stress relaxation within the bundle leading to short segments of one or more filaments yielding at the same time. This yield event was not observed for bundles in air.

This device fitted, with a thicker cantilever than the one used here, could also be used to investigate mechanical damage in fascicles extracted from rat tail tendons in PBS aqueous solution (Zitnay et al., 2017). The resolution provided by this instrument could allow the observation of slippage or partial failure events not detectable using standard tensile testers where the signal to noise ratio is not sufficiently high to allow such a detection. In addition, this device is capable of cyclic loading to investigate the accumulation of mechanical damage within the fascicle.

5. Conclusions

We have designed and validated an interferometric tensile tester capable of observing the signature of mechanical damage in a hierarchical material in air and in liquid. We demonstrated the force and time resolution of the system using collagen fibers with a hierarchical structure that mimics the one of a mammalian tendon. We were able to observe slippage and yield events that are undetectable with standard tensile testers opening the road for the study of mechanical damage in a broad range of materials including tissue engineering scaffold.

CRediT authorship contribution statement

Hessameddin Yaghoobi: Writing – original draft, Visualization, Validation, Methodology, Investigation, Formal analysis, Data curation, Conceptualization. **Chloe Tremblais:** Writing – review & editing, Visualization, Validation, Investigation, Formal analysis, Data curation. **Alex Gareau:** Writing – review & editing, Validation, Investigation, Formal analysis, Data curation. **Matthieu Cointe:** Writing – review & editing, Validation, Methodology, Investigation, Formal analysis, Data curation. **Alexey B. Tikhomirov:** Writing – review & editing, Validation, Software, Methodology. **Laurent Kreplak:** Writing – original draft, Visualization, Validation, Supervision, Resources, Methodology, Investigation, Funding acquisition, Formal analysis, Data curation, Conceptualization. **Daniel Labrie:** Writing – original draft, Visualization, Validation, Supervision, Resources, Methodology, Investigation, Funding acquisition, Formal analysis, Data curation, Conceptualization.

Declaration of competing interest

The following authors declare the following financial interests/personal relationships which may be considered as potential competing interests:H.Y. and L.K. report financial support provided by 3D BioFibR., a company commercializing advanced fiber technologies. LK consults with 3D BioFibR. and he has equity in 3D BioFibR.

Data availability

Data will be made available on request.

Acknowledgments

We would like to thank Florian Rispe, Antoine Lepers, Alex Godet and Augustin Westrelin for their technical support during the course of this project. This study was supported in part by funds from L.K., RGPIN/03781-2018 and ALLRP 561042-20 and by the Department of Physics and Atmospheric Science, Dalhousie University.

Appendix A. Supplementary data

Supplementary data to this article can be found online at https://doi.org/10.1016/j.jmbbm.2024.106467.

References

Andriotis, O.G., Desissaire, S., Thurner, P.J., 2018. Collagen fibrils: nature's highly tunable nonlinear springs. ACS Nano 12, 3671–3680. https://doi.org/10.1021/acsnano.8b00837.

Andriotis, O.G., Nalbach, M., Thurner, P.J., 2023. Mechanics of isolated individual collagen fibrils. Acta Biomaterialia, The Mechanics of Cells and Fibers 163, 35–49. https://doi.org/10.1016/j.actbio.2022.12.008.

Baldwin, SamuelJ., Kreplak, L., Lee, J.Michael, 2019. MMP-9 selectively cleaves non-D-banded material on collagen fibrils with discrete plasticity damage in mechanically-overloaded tendon. J. Mech. Behav. Biomed. Mater. 95, 67–75. https://doi.org/10.1016/j.jmbbm.2019.03.020.

Chambers, N.C., Herod, T.W., Veres, S.P., 2018. Ultrastructure of tendon rupture depends on strain rate and tendon type. J. Orthop. Res. 36, 2842–2850. https://doi.org/10.1002/jor.24067.

Chowdhry, G., Chang, Y.M., Frampton, J.P., Kreplak, L., 2021. Polymer entanglement drives formation of fibers from stable liquid bridges of highly viscous dextran solutions. Soft Matter 17, 1873–1880. https://doi.org/10.1039/d0sm01550d.

Herod, T.W., Chambers, N.C., Veres, S.P., 2016. Collagen fibrils in functionally distinct tendons have differing structural responses to tendon rupture and fatigue loading. Acta Biomater. 42, 296–307. https://doi.org/10.1016/j.actbio.2016.06.017.

Hijazi, K.M., Singfield, K.L., Veres, S.P., 2019. Ultrastructural response of tendon to excessive level or duration of tensile load supports that collagen fibrils are mechanically continuous. J. Mech. Behav. Biomed. Mater. 97, 30–40. https://doi.org/10.1016/j.jmbbm.2019.05.002.

Iqbal, S.M.A., Deska-Gauthier, D., Kreplak, L., 2019. Assessing collagen fibrils molecular damage after a single stretch-release cycle. Soft Matter 15, 6237–6246. https://doi.org/10.1039/c9sm00832b.

Jericho, S.K., Jericho, M.H., 2002. Device for the determination of spring constants of atomic force microscope cantilevers and micromachined springs. Rev. Sci. Instrum. 73, 2483–2485. https://doi.org/10.1063/1.1471351.

Li, X., Zhang, Q., Yu, S.M., Li, Y., 2023. The chemistry and biology of collagen hybridization. J. Am. Chem. Soc. 145, 10901–10916. https://doi.org/10.1021/jacs.3c00713.

Lifshitz, E.M., Kosevich, A.M., Pitaevskii, L.P., 1986. Chapter II - the equilibrium of rods and plates. In: Lifshitz, E.M., Kosevich, A.M., Pitaevskii, L.P. (Eds.), Theory of Elasticity, third ed. Butterworth-Heinemann, Oxford, pp. 38–86. https://doi.org/10.1016/B978-0-08-057069-3.50009-7.

Lin, A.H., Allan, A.N., Zitnay, J.L., Kessler, J.L., Yu, S.M., Weiss, J.A., 2020. Collagen denaturation is initiated upon tissue yield in both positional and energy-storing tendons. Acta Biomater. 118, 153–160. https://doi.org/10.1016/j.actbio.2020.09.056.

Palit, S., Kreplak, L., Frampton, J.P., 2022. Formation of core-sheath polymer fibers by free surface spinning of aqueous two-phase systems. Langmuir 38, 4617–4624. https://doi.org/10.1021/acs.langmuir.1c03472.

Peacock, C., Lee, E., Beral, T., Cisek, R., Tokarz, D., Kreplak, L., 2020. Buckling and torsional instabilities of a nanoscale biological rope bound to an elastic substrate. ACS Nano 14, 12877–12884. https://doi.org/10.1021/acsnano.0c03695.

Quigley, A.S., Bancelin, S., Deska-Gauthier, D., Légaré, F., Kreplak, L., Veres, S.P., 2018. In tendons, differing physiological requirements lead to functionally distinct nanostructures. Sci. Rep. 8, 4409. https://doi.org/10.1038/s41598-018-22741-8.

Revell, C.K., Jensen, O.E., Shearer, T., Lu, Y., Holmes, D.F., Kadler, K.E., 2021. Collagen fibril assembly: new approaches to unanswered questions. Matrix Biol. 12, 100079 https://doi.org/10.1016/j.mbplus.2021.100079.

Ryu, S., Chou, J.B., Lee, K., Lee, D., Hong, S.H., Zhao, R., Lee, H., Kim, S., 2015. Direct insulation-to-conduction transformation of adhesive catecholamine for simultaneous increases of electrical conductivity and mechanical strength of CNT fibers. Adv. Mater. 27, 3250–3255. https://doi.org/10.1002/adma.201500914.

Sahota, J.K., Gupta, N., Dhawan, D., 2020. Fiber Bragg grating sensors for monitoring of physical parameters: a comprehensive review. Opt. Eng. 59, 1. https://doi.org/10.1117/1.OE.59.6.060901.

Snedeker, J.G., Foolen, J., 2017. Tendon injury and repair – a perspective on the basic mechanisms of tendon disease and future clinical therapy. Acta Biomater. 63, 18–36. https://doi.org/10.1016/j.actbio.2017.08.032.

Svensson, R.B., Herchenhan, A., Starborg, T., Larsen, M., Kadler, K.E., Qvortrup, K., Magnusson, S.P., 2017. Evidence of structurally continuous collagen fibrils in tendons. Acta Biomater. 50, 293–301. https://doi.org/10.1016/j.actbio.2017.01.006.

Svensson, R.B., Mulder, H., Kovanen, V., Magnusson, S.P., 2013. Fracture mechanics of collagen fibrils: influence of natural cross-links. Biophys. J. 104, 2476–2484. https://doi.org/10.1016/j.bpj.2013.04.033.

Svensson, R.B., Smith, S.T., Moyer, P.J., Magnusson, S.P., 2018. Effects of maturation and advanced glycation on tensile mechanics of collagen fibrils from rat tail and Achilles tendons. Acta Biomater. 70, 270–280. https://doi.org/10.1016/j.actbio.2018.02.005.

Szczesny, S.E., Aeppli, C., David, A., Mauck, R.L., 2018. Fatigue loading of tendon results in collagen kinking and denaturation but does not change local tissue mechanics. J. Biomech. 71, 251–256. https://doi.org/10.1016/j.jbiomech.2018.02.014.

Szczesny, S.E., Elliott, D.M., 2014. Interfibrillar shear stress is the loading mechanism of collagen fibrils in tendon. Acta Biomater. 10, 2582–2590. https://doi.org/10.1016/j.actbio.2014.01.032.

Tarnutzer, K., Siva Sankar, D., Dengjel, J., Ewald, C.Y., 2023. Collagen constitutes about 12% in females and 17% in males of the total protein in mice. Sci. Rep. 13, 4490. https://doi.org/10.1038/s41598-023-31566-z.

Veres, S.P., Harrison, J.M., Lee, J.M., 2013. Repeated subrupture overload causes progression of nanoscaled discrete plasticity damage in tendon collagen fibrils. J. Orthop. Res. 31, 731–737. https://doi.org/10.1002/jor.22292.

Veres, S.P., Lee, J.M., 2012. Designed to fail: a novel mode of collagen fibril disruption and its relevance to tissue toughness. Biophys. J. 102, 2876–2884. https://doi.org/10.1016/j.bpj.2012.05.022.

Verma, S.K., Yaghoobi, H., Slaine, P., Baldwin, S.J., Rainey, J.K., Kreplak, L., Frampton, J.P., 2022. Multi-pin contact drawing enables production of anisotropic collagen fiber substrates for alignment of fibroblasts and monocytes. Colloids Surf. B Biointerfaces 215, 112525. https://doi.org/10.1016/j.colsurfb.2022.112525.

Yaghoobi, H., Clarke, A., Kerr, G., Frampton, J., Kreplak, L., 2023. Multifilament collagen fiber bundles with tendon-like structure and mechanical performance. Macromol. Rapid Commun. 2300204, 1–11. https://doi.org/10.1002/marc.202300204.

Yang, W., 2015. On the tear resistance of skin. Nat. Commun. 10.

Zhu, C., Zheng, H., Ma, L., Yao, Z., Liu, B., Huang, J., Rao, Y., 2023. Advances in fiber-optic extrinsic fabry–perot interferometric physical and mechanical sensors: a review. IEEE Sensor. J. 23, 6406–6426. https://doi.org/10.1109/JSEN.2023.3244820.

Zitnay, J.L., Li, Y., Qin, Z., San, B.H., Depalle, B., Reese, S.P., Buehler, M.J., Yu, S.M., Weiss, J.A., 2017. Molecular level detection and localization of mechanical damage in collagen enabled by collagen hybridizing peptides. Nat. Commun. 8, 14913 https://doi.org/10.1038/ncomms14913.